Snow precipitation on Mars driven by cloud-induced night-time convection

Aymeric Spiga[1]*, David P. Hinson[2,3], Jean-Baptiste Madeleine[1], Thomas Navarro[1], Ehouarn Millour[1], François Forget[1] and Franck Montmessin[4]

Although it contains less water vapour than Earth's atmosphere, the Martian atmosphere hosts clouds. These clouds, composed of water-ice particles, influence the global transport of water vapour and the seasonal variations of ice deposits. However, the influence of water-ice clouds on local weather is unclear: it is thought that Martian clouds are devoid of moist convective motions, and snow precipitation occurs only by the slow sedimentation of individual particles. Here we present numerical simulations of the meteorology in Martian cloudy regions that demonstrate that localized convective snowstorms can occur on Mars. We show that such snowstorms—or ice microbursts—can explain deep night-time mixing layers detected from orbit and precipitation signatures detected below water-ice clouds by the Phoenix lander. In our simulations, convective snowstorms occur only during the Martian night, and result from atmospheric instability due to radiative cooling of water-ice cloud particles. This triggers strong convective plumes within and below clouds, with fast snow precipitation resulting from the vigorous descending currents. Night-time convection in Martian water-ice clouds and the associated snow precipitation lead to transport of water both above and below the mixing layers, and thus would affect Mars' water cycle past and present, especially under the high-obliquity conditions associated with a more intense water cycle.

Martian water-ice clouds were one of the first atmospheric phenomena to be observed on Mars[1–3]. The absolute quantity of water vapour is much smaller on Mars than it is on the Earth (a few precipitable micrometers, $1 \, \text{pr-}\mu\text{m} = 1 \, \text{g m}^{-2}$); yet the low pressure and temperature of the Martian atmosphere cause the relative humidity to often reach saturation conditions, leading to the formation of water-ice clouds[4]. Water-ice clouds on Mars exhibit seasonal[5,6] and diurnal[7] variability, with the formation of a tropical cloud belt during the aphelion seasons and 'polar hood' clouds at high latitudes in fall/spring[8,9]. Their infrared absorption and emission dominate scattering and absorption in the visible[10], thereby warming the daytime upper troposphere of Mars[11] and, most significantly, cooling the atmosphere and warming the surface at night (up to $+25 \, \text{K}$) (refs 12,13).

Night-time mixing layers and cloud-induced convection

Night-time temperature inversions are found in radio-occultation profiles obtained with Mars Global Surveyor (MGS)[14] and Mars Reconnaissance Orbiter (MRO)[15] in regions covered with water-ice clouds. Recasting the radio-occultation temperature profiles in potential temperature θ (that is, temperature corrected for adiabatic effects) revealed that, unexpectedly, the night-time temperature inversions are so pronounced that the resulting layers are convectively neutral[15] ($\partial\theta/\partial z = 0$, where z is altitude, see the orange profile in Fig. 1b), requiring mixing processes to occur over a $\sim$8-km-deep layer in the Martian troposphere at 2–3 AM local time. The origin of these enigmatic night-time mixing layers has remained elusive thus far. Their regions of occurrence (Fig. 1a: Arabia/Syrtis Major, Elysium, Tharsis) correlate with locations where: extensive

water-ice cloud formation is regularly observed[12,16,17]; the daytime convective boundary layer is particularly deep[18,19]; atmospheric tides impact the thermal structure[14,20]; and the gravity wave activity is significant[21]. Night-time mixing layers cannot be the remainder of the mixing layers from the daytime convective boundary layer, which disappear a few hours after sunset[15]; and they are both too deep and too low in the Martian troposphere to be caused by the breaking of atmospheric tides and/or gravity waves, according to existing modelling and observations[22]. Thus, the only plausible origin of the deep night-time mixing layers is aphelion water-ice clouds. However, the properties of the mixing layers evidenced in the observations (regionally confined, extremely deep, convectively neutral) are not reproduced by existing Global Climate Models[15] (GCM), in spite of both the formation and radiative impact of water-ice clouds being accounted for in these models[12,13].

To better understand the processes at work within these Martian clouds, we use a mesoscale atmospheric model[23–25], which computes the three-dimensional evolution of the atmospheric state in a specific region of interest enclosing Tharsis Montes and Amazonis Planitia, at finer spatial resolution (30 km in the horizontal and 750 m in the vertical dimensions) and using more sophisticated cloud modelling[13,26] than the GCM in ref. 15 (see Methods).

Our mesoscale simulations reproduce night-time mixing layers in agreement with those found in radio-occultations[15] (Fig. 1b). The model reproduces both the vertical extent (8 km) and the altitude of occurrence (5–10 km) of observed mixing layer's in Tharsis Montes (Fig. 1c), contrary to GCM simulations in ref. 15 where <2-km-deep mixing layers were obtained at an altitude of 10 km. Our mesoscale simulations also reproduce the lack of mixing layers in

1

Figure 1 | Night-time mixing layers detected in radio-occultations from orbit are reproduced by mesoscale simulations. a, Circles on a MOLA topography map indicate MGS radio-occultation measurements (methodology in refs 14,15) in Martian Year 28 aphelion season ($L_s = 68°–109°$), coloured in pink if a mixing layer is observed; coloured squares locate the profiles shown in **b** and **c**. **b**, Pre-dawn potential temperature profiles in MGS radio-occultations in Tharsis Montes (orange) and Amazonis Planitia (blue) at $L_s = 140°$ in Martian Year 24, from ref. 15. **c**, Potential temperature profiles, simulated by our mesoscale model, at the same season, local time and regions as in **b**.

Amazonis Planitia where, contrary to Tharsis Montes, no water-ice cloud is present at night[12] (Fig. 1c). Figure 2a demonstrates that the radiative effect of water-ice clouds strongly affects the thermal structure within and below the cloud and causes the observed deep night-time mixing layers (evidenced as quasi-vertical contours of potential temperature). Simulations without the radiative effect of water-ice clouds do not exhibit those mixing layers (Fig. 2a and Supplementary Fig. 1). Gravity waves resolved by our mesoscale simulations produce mixing layers with much thinner vertical extent and higher altitude of occurrence than the observed mixing layers.

Convective mixing associated with water-ice clouds on Mars is driven by a distinctly different mechanism than daytime convection in the Planetary Boundary Layer[19]. Air parcels become negatively buoyant because the cloud layer is cooling radiatively, which explains why the mixing layers appear mostly below the water-ice cloud. This is analogous to the negative buoyancy associated with radiative cooling by marine boundary layer clouds on Earth[27], although the resulting mixing layers are much thicker on Mars. Our model indicates that the net radiative cooling rate from thermal infrared emission within Martian water-ice clouds reaches 4 K per hour (Supplementary Fig. 1), which means that it takes only a few hours after sunset for the atmosphere to reach convective instability. Conversely, in the Martian daytime, the absorption of incoming sunlight by water-ice clouds stabilizes the atmosphere, thereby preventing the formation of convectively

unstable layers in the troposphere. The combination of convective motions fuelled by negative buoyancy, and night-time conditions more propitious for strong convection than in daytime[28], make Mars' water-ice clouds analogous to Venus' sulfuric-acid clouds.

Convective snowstorms and the Phoenix lidar observations

The putative convective motions driven by radiative destabilization that create the night-time mixing layers are not resolved by our mesoscale simulations, in which mixing layers result from parameterized mixing obtained by a combination of a dry adiabatic adjustment scheme[23,29] and a local diffusion scheme[30]. Vertical winds are negligible within the night-time mixing layers reproduced by mesoscale modelling; they are significant only in the vicinity of Tharsis volcanoes' slope (katabatic winds[31]) and in gravity waves propagating towards the higher troposphere[32]. To further characterize the small-scale circulations underlying the Martian night-time mixing layers, we carried out turbulence-resolving Large-Eddy Simulations (LES) at spatial resolutions of 100–200 m with the same radiative, microphysical and transport schemes[13,26] as in the mesoscale simulations (see Methods for a detailed description of LES).

Our LES shown in Fig. 2b demonstrate that the Martian night-time troposphere is highly turbulent within and below water-ice clouds, in great contrast with the (hitherto believed) lack of convection in Martian water-ice clouds ensuing from their weak
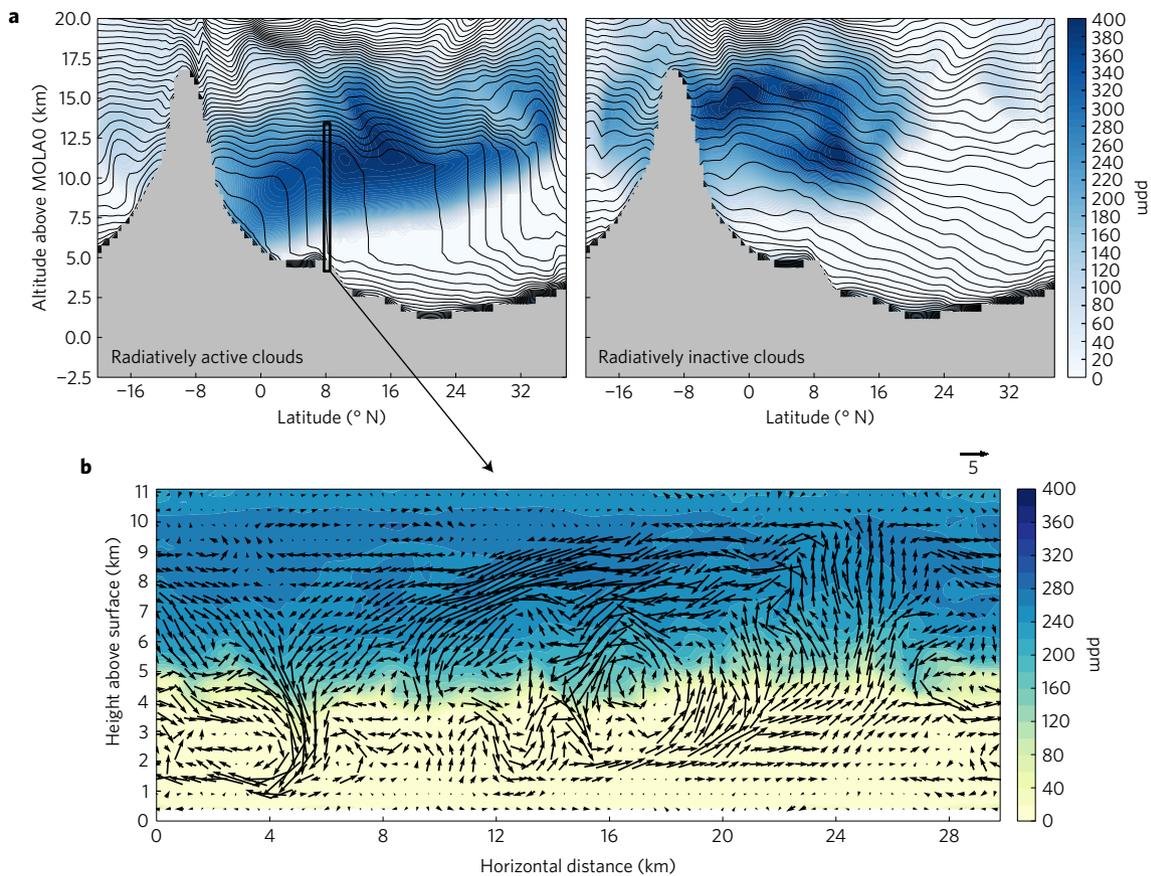
Figure 2 | The radiative effect of water-ice clouds at night triggers powerful convective plumes causing deep mixing layers and ice microbursts.
a, Water-ice volumetric mixing ratio (shaded) and potential temperature (contours) simulated by mesoscale modelling with (top left) and without (top right) radiatively active water-ice clouds, at the longitude of Arsia Mons (−120° E), the season of the aphelion cloud belt ($L_s = 120°$), and the local time of radio-occultations (∼3 AM). **b**, Typical water-ice volumetric mixing ratio (shaded) and convective winds (vectors, shown every two grid points) from LES with radiatively active water-ice clouds in environmental conditions corresponding to the region indicated in **a**.

latent heating[4,8]. After a few simulated Martian hours, powerful ascending and descending plumes develop as a result of the convectively unstable conditions caused by radiative cooling of water-ice particles within the cloud (Fig. 2b and Supplementary Fig. 2). A 8-km mixing layer within and below a 3-km-deep water-ice cloud, analogous to the radio-occultations and the mesoscale simulations (Fig. 1b,c), is reproduced by our LES as a result of the vigorous mixing by the resolved turbulent convective motions (see Supplementary Fig. 3 and Methods). The vertical wind velocities reach $\pm 10\,\mathrm{m\,s^{-1}}$, meaning that night-time convection below water-ice clouds is as vigorous as what is encountered in the daytime convective Planetary Boundary Layer on Mars[19] and twice stronger than the values measured by balloons in the Venusian convective cloud layer[33]. This is also comparable to typical vertical motions in the bulk of a maturing terrestrial cumulus[34]. In our LES of night-time Martian water-ice clouds, the turbulent horizontal wind velocities reach about the same values as vertical velocities. Turbulent wind gusts can be powerful down to 5 km below the cloud, but do not reach the surface, owing to the stable near-surface layer imposed by the radiative cooling of the surface at night (Fig. 1b). Just as it is the case on Earth[35], the strong horizontal and vertical convective currents developing below water clouds at night on Mars could be a source of atmospheric hazards for the robotic and human exploration of the Red Planet.

Descending plumes below the water-ice cloud generate a significant downward transport of water-ice particles, resulting in ∼2-km-deep virga-like structures at the bottom of the cloud (Fig. 2b). This rapid downward transport cannot be achieved

by sedimentation: the radii of the ice cloud particles range between 3 and 4 μm, which entail sedimentation fall velocities of $\sim 10^{-2}\,\mathrm{m\,s^{-1}}$. We suggest to name 'Martian water-ice microbursts' the rapid, convective, downward transport of water-ice particles at night on Mars, drawing analogy with terrestrial microbursts, which are rapid subsidences of cold dense air from a convective cloud[35], often associated with precipitation and the occurrence of virga-like structures. To highlight that night-time convection below water-ice clouds is a new mechanism for snow precipitation on Mars, we also propose to use the term 'convective snowstorms'. The water-ice particles in Martian convective snowstorms sublimate through the strong adiabatic warming associated with downward convective motions. Thus, precipitating water-ice particles from Martian convective snowstorms at night only reach the surface if the cloud is ∼1–2 km from the surface—that is, the vertical extent of a simulated virga.

The modelled virga-like structures formed by night-time convective snowstorms are strongly reminiscent of the fall streaks detected below a night-time water-ice cloud by the LIDAR on board the Mars Phoenix lander[36,37] (Fig. 3a). Those were interpreted by static microphysical modelling[38] as sedimentation streaks formed by 30–50 μm water-ice particles falling over a 1.2-km height in 4 h. We propose a different interpretation by applying our convection-resolving model to the environmental conditions met by the Phoenix LIDAR when observing fall streaks. All the characteristics of the virga and fall streaks observed by the Phoenix LIDAR (vertical extent, morphology and frequency) are reproduced by our model (Fig. 3b). We thereby demonstrate that the virga and fall streaks detected by
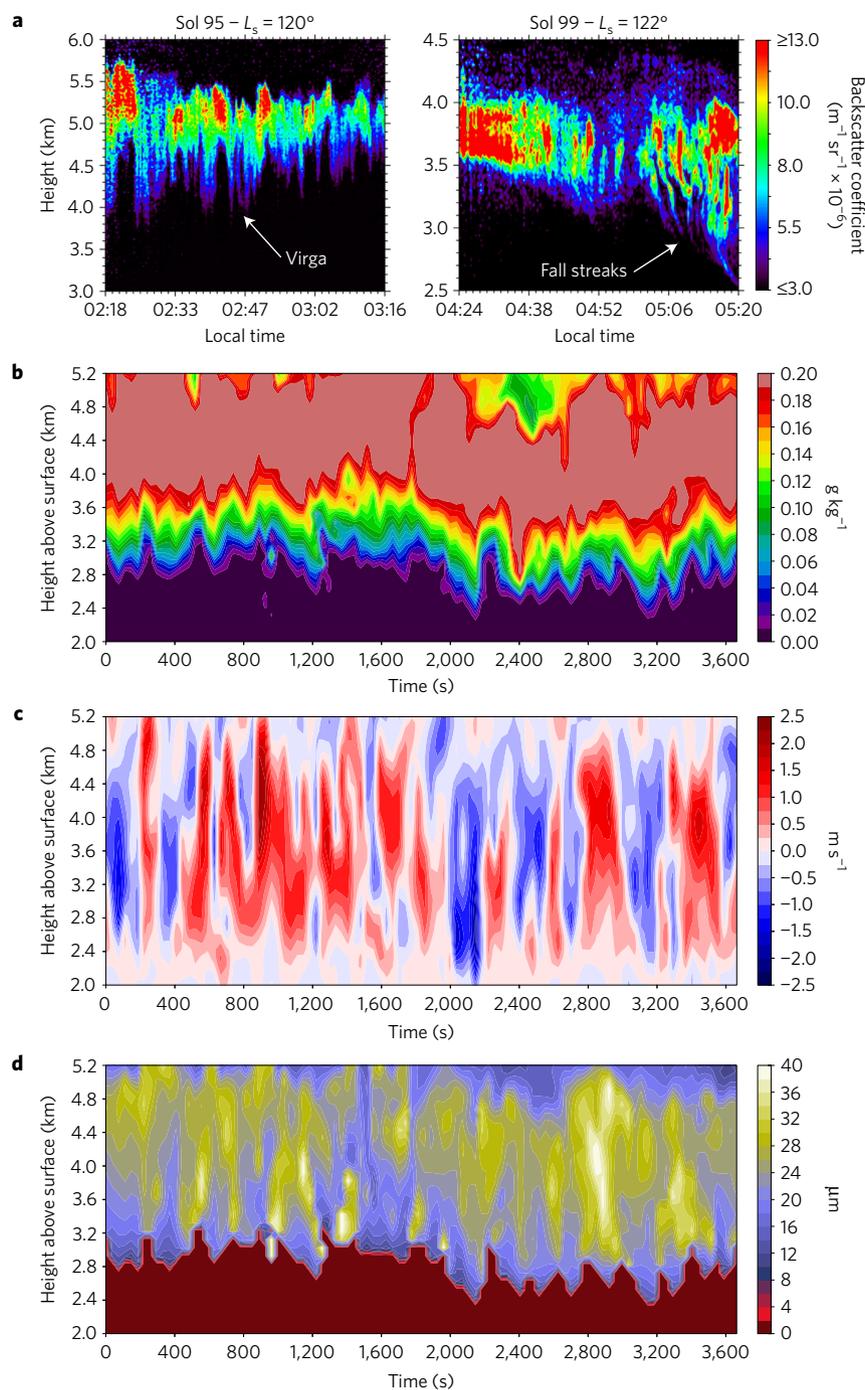
Figure 3 | Water-ice convective microbursts provide a straightforward explanation for snow precipitation evidenced by the Phoenix LIDAR. a–d, Results from LES with radiatively active water-ice clouds, carried out in the environmental conditions where and when virga and fall streaks were witnessed by the LIDAR on board the Mars Phoenix lander (subplot **a** from refs 36,37). Fields are displayed over the vertical and temporal dimensions: water-ice mass mixing ratio (**b**), vertical velocity (**c**) and particle radii of water-ice particles (**d**).

Phoenix are formed by $2\,\mathrm{m\,s^{-1}}$ downward plumes (Fig. 3b). The predicted sizes of water-ice particles in our simulations are similar to those in static microphysical simulations[38] (30–40 μm, see Fig. 3d); the key novelty provided by our dynamical simulations is that, thanks to convective motions, their characteristic fall time is much faster than hitherto believed[36,38], several hundreds seconds rather than several hours (the sedimentation fall velocity of a 40 μm-sized water-ice particle is no larger than $0.2\,\mathrm{m\,s^{-1}}$). Precipitation by convective microbursts provides a more straightforward mechanism than sedimentation to explain the snow precipitation witnessed by the Phoenix lander on Mars.

Implications for contemporary and past water cycles

The fact that convective plumes develop within and below Martian water-ice clouds at night means that, in stark contrast to what has been assumed thus far[8], mixing in the Martian troposphere is strongly impacted by water-ice clouds. To correctly predict the deep night-time mixing layers, and their impact on the mixing of heat, momentum, aerosols and volatiles in the Martian atmosphere, Martian climate models will need not only to account for the radiative effect of water-ice clouds[12,13], but also to employ finer horizontal and vertical resolutions than the current standards[8,9,15,26].

Convective snowstorms have a strong impact on the vertical distribution of water in the lower atmosphere of Mars (see Supplementary Figs 3 and 4, and the related discussion in the Methods). Our LES demonstrate that, on average, the convective plumes induced by water-ice clouds at night cause a downward transport of water ice below the cloud, an upward transport of water vapour within the cloud, through the hygropause (the level above which the water vapour mixing ratio rapidly declines), and a net transport of total water (vapour and ice) outside the mixing layers. We cannot conclude, however, whether this net transport of water is in favour of the near-surface atmosphere or the higher troposphere. Further work is needed to determine if convective microbursts in water-ice clouds on Mars could enhance or mitigate the 'Clancy effect'[5]—the potential ability of water-ice clouds to confine water below the return branch of the solsticial Hadley cell on Mars[9]. Solving this question is key to understanding the stability of the past and current water cycles on Mars, since the escape of water vapour to space strongly depends on how much water could be transported towards the higher troposphere and lower mesosphere[39,40].

The new mechanism we describe herein for snow precipitation on Mars has implications too for the climate of Mars in the recent past when, in pressure conditions close to the present state, water-ice precipitation played a key role in forming tropical and mid-latitude glaciers on Mars under high-obliquity conditions[41,42].

Methods

Methods, including statements of data availability and any associated accession codes and references, are available in the online version of this paper.

References

1. Herschel, W. On the remarkable appearance of the polar regions of the planet Mars, the inclination of its axis, the position of its poles, and its spheroidical figure; with a few hints relative to its diameter. *Phil. Trans.* **24**, 233–273 (1784).
2. Curran, R. J., Conrath, B. J., Hanel, R. A., Kunde, V. G. & Pearl, J. C. Mars: Mariner 9 spectroscopic evidence for H_2O ice clouds. *Science* **182**, 381–383 (1973).
3. Kahn, R. The spatial and seasonal distribution of Martian clouds and some meteorological implications. *J. Geophys. Res.* **89**, 6671–6688 (1984).
4. Savijärvi, H. & Määttänen, A. Boundary-layer simulations for the Mars Phoenix lander site. *Q. J. R. Meteorol. Soc.* **136**, 1497–1505 (2010).
5. Clancy, R. T. *et al.* Water vapor saturation at low altitudes around Mars aphelion: a key to Mars climate. *Icarus* **122**, 36–62 (1996).
6. Wang, H. & Ingersoll, A. P. Martian clouds observed by Mars Global Surveyor Mars Orbiter Camera. *J. Geophys. Res.* **107**, 5078 (2002).
7. Madeleine, J.-B. *et al.* Aphelion water-ice cloud mapping and property retrieval using the OMEGA imaging spectrometer onboard Mars Express. *J. Geophys. Res.* **117**, E00J07 (2012).
8. Richardson, M. I., Wilson, R. J. & Rodin, A. V. Water ice clouds in the Martian atmosphere: general circulation model experiments with a simple cloud scheme. *J. Geophys. Res.* **107**, 5064 (2002).
9. Montmessin, F., Forget, F., Rannou, P., Cabane, M. & Haberle, R. M. Origin and role of water ice clouds in the Martian water cycle as inferred from a general circulation model. *J. Geophys. Res.* **109**, 10004 (2004).
10. Colaprete, A. & Toon, O. B. The radiative effects of Martian water ice clouds on the local atmospheric temperature profile. *Icarus* **145**, 524–532 (2000).
11. Wilson, R. J., Lewis, S. R., Montabone, L. & Smith, M. D. Influence of water ice clouds on Martian tropical atmospheric temperatures. *Geophys. Res. Lett.* **35**, 7202 (2008).
12. Wilson, R. J., Neumann, G. A. & Smith, M. D. Diurnal variation and radiative influence of Martian water ice clouds. *Geophys. Res. Lett.* **34**, 2710 (2007).
13. Madeleine, J.-B., Forget, F., Millour, E., Navarro, T. & Spiga, A. The influence of radiatively active water ice clouds on the Martian climate. *Geophys. Res. Lett.* **39**, L23202 (2012).
14. Hinson, D. P. & Wilson, R. J. Temperature inversions, thermal tides, and water ice clouds in the Martian tropics. *J. Geophys. Res.* **109**, 1002 (2004).
15. Hinson, D. P. *et al.* Initial results from radio occultation measurements with the Mars Reconnaissance Orbiter: a nocturnal mixed layer in the tropics and comparisons with polar profiles from the Mars Climate Sounder. *Icarus* **243**, 91–103 (2014).
16. Smith, M. D. Interannual variability in TES atmospheric observations of Mars during 1999–2003. *Icarus* **167**, 148–165 (2004).
17. Pankine, A. A., Tamppari, L. K., Bandfield, J. L., McConnochie, T. H. & Smith, M. D. Retrievals of martian atmospheric opacities from MGS TES nighttime data. *Icarus* **226**, 708–722 (2013).
18. Hinson, D. P., Pätzold, M., Tellmann, S., Häusler, B. & Tyler, G. L. The depth of the convective boundary layer on Mars. *Icarus* **198**, 57–66 (2008).
19. Spiga, A., Forget, F., Lewis, S. R. & Hinson, D. P. Structure and dynamics of the convective boundary layer on Mars as inferred from Large-Eddy Simulations and remote-sensing measurements. *Q. J. R. Meteorol. Soc.* **136**, 414–428 (2010).
20. Wilson, R. W. & Hamilton, K. Comprehensive model simulation of thermal tides in the Martian atmosphere. *J. Atmos. Sci.* **53**, 1290–1326 (1996).
21. Creasey, J. E., Forbes, J. M. & Hinson, D. P. Global and seasonal distribution of gravity wave activity in Mars' lower atmosphere derived from MGS radio occultation data. *Geophys. Res. Lett.* **33**, 1803 (2006).
22. Lee, C. *et al.* Thermal tides in the Martian middle atmosphere as seen by the Mars Climate Sounder. *J. Geophys. Res.* **114**, E03005 (2009).
23. Spiga, A. & Forget, F. A new model to simulate the Martian mesoscale and microscale atmospheric circulation: validation and first results. *J. Geophys. Res.* **114**, E02009 (2009).
24. Spiga, A., Faure, J., Madeleine, J.-B., Määttänen, A. & Forget, F. Rocket dust storms and detached dust layers in the Martian atmosphere. *J. Geophys. Res.* **118**, 746–767 (2013).
25. Skamarock, W. C. & Klemp, J. B. A time-split nonhydrostatic atmospheric model for weather research and forecasting applications. *J. Comput. Phys.* **227**, 3465–3485 (2008).
26. Navarro, T. *et al.* Global climate modeling of the Martian water cycle with improved microphysics and radiatively active water ice clouds. *J. Geophys. Res.* **119**, 1479–1495 (2014).
27. Nicholls, S. The structure of radiatively driven convection in stratocumulus. *Q. J. R. Meteorol. Soc.* **115**, 487–511 (1989).
28. Imamura, T. *et al.* Inverse insolation dependence of Venus' cloud-level convection. *Icarus* **228**, 181–188 (2014).
29. Hourdin, F., Le Van, P., Forget, F. & Talagrand, O. Meteorological variability and the annual surface pressure cycle on Mars. *J. Atmos. Sci.* **50**, 3625–3640 (1993).
30. Hourdin, F., Couvreux, F. & Menut, L. Parameterization of the dry convective boundary layer based on a mass flux representation of thermals. *J. Atmos. Sci.* **59**, 1105–1123 (2002).
31. Spiga, A. *et al.* The impact of Martian mesoscale winds on surface temperature and on the determination of thermal inertia. *Icarus* **212**, 504–519 (2011).
32. Michaels, T. I., Colaprete, A. & Rafkin, S. C. R. Significant vertical water transport by mountain-induced circulations on Mars. *Geophys. Res. Lett.* **33**, L16201 (2006).
33. Linkin, V. M. *et al.* VEGA balloon dynamics and vertical winds in the Venus middle cloud region. *Science* **231**, 1417–1419 (1986).
34. Byers, H. R. & Braham, R. R. Jr Thunderstorm structure and circulation. *J. Meteorol.* **5**, 71–86 (1948).
35. Wakimoto, R. M. & Bringi, V. N. Dual-polarization observations of microbursts associated with intense convection: the 20 July storm during the MIST project. *Mon. Weather Rev.* **116**, 1521–1539 (1988).
36. Whiteway, J. A. *et al.* Mars water-ice clouds and precipitation. *Science* **325**, 68–70 (2009).
37. Dickinson, C. *et al.* Lidar atmospheric measurements on Mars and Earth. *Planet. Space Sci.* **59**, 942–951 (2011).
38. Daerden, F. *et al.* Simulating observed boundary layer clouds on Mars. *Geophys. Res. Lett.* **37**, L04203 (2010).
39. Maltagliati, L. *et al.* Evidence of water vapor in excess of saturation in the atmosphere of Mars. *Science* **333**, 1868–1871 (2011).
40. Chaffin, M. S., Deighan, J., Schneider, N. M. & Stewart, A. I. F. Elevated atmospheric escape of atomic hydrogen from Mars induced by high-altitude water. *Nat. Geosci.* **10**, 174–178 (2017).
41. Forget, F., Haberle, R. M., Montmessin, F., Levrard, B. & Head, J. W. Formation of glaciers on Mars by atmospheric precipitation at high obliquity. *Science* **311**, 368–371 (2006).
42. Madeleine, J.-B. *et al.* Amazonian northern mid-latitude glaciation on Mars: a proposed climate scenario. *Icarus* **203**, 390–405 (2009).

Acknowledgements

Author contributions

All authors contributed to the scientific discussions and manuscript writing. A.S. designed the study, developed the mesoscale model and Large-Eddy Simulations (LES) for Mars, performed all computer runs, and led manuscript writing. D.P.H. provided and analysed the radio-occultations measurements of night-time mixing layers. J.-B.M. and F.F. developed and validated the radiative model for dust and water-ice particles. T.N. and J.-B.M. developed and validated the microphysical water-ice cloud model. E.M. led the development and validation of the physical packages in the Global Climate Model and mesoscale model. F.F. and F.M. provided expertise on atmospheric modelling of Martian water-ice clouds.

Additional information

Supplementary information is available in the online version of the paper. Reprints and permissions information is available online at www.nature.com/reprints. Publisher's note: Springer Nature remains neutral with regard to jurisdictional claims in published maps and institutional affiliations. Correspondence and requests for materials should be addressed to A.S.

Competing financial interests

The authors declare no competing financial interests.

Methods

Mesoscale simulations. We employ the Laboratoire de Météorologie Dynamique (LMD) Martian Mesoscale Model[23,24] (MMM) to carry out three-dimensional numerical modelling of the Martian atmosphere at high spatial resolution in a specific region of interest. Our LMD-MMM relies on a fully compressible, non-hydrostatic hydrodynamical solver (integrating the Navier–Stokes equations for the rotating atmospheric fluid) borrowed from the terrestrial mesoscale model Weather Research and Forecast[25] (WRF). The LMD-MMM consists in coupling this hydrodynamical solver (using planetary constants and calendar adapted to Mars) with the physical packages developed in the LMD Martian Global Climate Model[43] (MGCM) to account for the physical phenomena left unresolved by the hydrodynamical solver (radiative transfer, small-scale turbulence, cloud microphysics). Initial and boundary conditions for the LMD-MMM are extracted from LMD-MGCM simulations[13,26] which use the exact same physical packages. The extent of the simulation domain in the LMD-MMM is chosen to ensure that the atmospheric fields predicted for at least 12 LMD-MGCM grid points are used as boundary conditions in each horizontal direction.

Radiative transfer in the LMD-MMM and LMD-MGCM accounts for infrared absorption/emission by CO_2 gas[44], dust particles[45] and water-ice particles[13], as well as visible absorption by the last two species. The radiative transfer model has the capability to run with and without the radiative effect of water-ice clouds included, to unambiguously evidence the radiative impact of these clouds. The size distribution of aerosol particles (dust, cloud ice, and dust as condensation nuclei in cloud ice) is modelled by a two-moment scheme, where each of the two moments (that is, mass mixing ratio and number density) related to the three kinds of aerosol particles is advected as a tracer in the hydrodynamical solver. As it is the case for temperature and winds, the initial and boundary conditions for those six tracers in the LMD-MMM are provided by LMD-MGCM simulations[13,26].

A detailed microphysical scheme is used to simulate the formation of water-ice clouds[26]. Once the saturation pressure is reached, the water vapour phase does not suddenly turn into a condensed phase: water-ice particles nucleate and grow onto airborne dust[46], and the nucleation rate determines the number of dust nuclei onto which water vapour will condense. Thus, predictions for water vapour and ice mixing ratios, as well as cloud particle sizes, are physically self-consistent; and, should dust nuclei be too rare, supersaturation[39] can be accounted for by the microphysical scheme. In our LMD-MMM runs, both condensation and sedimentation laws for water-ice particles are exactly similar as in the previously published LMD-MGCM studies of water-ice clouds[9,13,26].

The mixing layers arising from unresolved turbulence in superadiabatic conditions (that is, $\partial\theta/\partial z < 0$) are produced in the LMD-MMM by a combination of two subgrid-scale parameterizations: a Mellor–Yamada diffusion scheme to represent vertical mixing by small-scale local turbulence (see ref. 30, appendix B) and a dry adiabatic adjustment scheme[29] to turn any remaining unstable layer $\partial\theta/\partial z < 0$ into a neutral equivalent $\partial\theta/\partial z = 0$ (without computing the intensity of the convective plumes which produce the mixing layer). To parameterize the daytime convective Planetary Boundary Layer (PBL) in the LMD-MMM, the dry adiabatic adjustment scheme has been replaced recently by a physically based 'thermal plume' model[47], accounting for the impact of the deepest non-local convective plumes; this 'thermal plume' model is, however, specifically designed for daytime PBL convective mixing and not employed to produce cloud-induced night-time mixing layers in the LMD-MMM simulations.

We perform LMD-MMM simulations in a domain that encloses the regions of Tharsis Montes and Eastern Amazonis Planitia and comprises $121 \times 121 \times 61$ grid points along the two horizontal and the vertical dimensions, with a mesh spacing of 30 km in the horizontal and ~750 m in the vertical (the model top is located at an approximate altitude of 42 km above the surface). The spatial resolutions we adopt in our mesoscale simulations are about a factor of 10 finer than GCMs in the three directions. Our LMD-MMM simulations are carried out in the aphelion cloud belt season, at two heliocentric longitudes $L_s = 120°$ (a canonical value for the aphelion belt season which is often used in the literature to compare cloud modelling and observations[12,48]) and $L_s = 140°$ (used to compare directly our mesoscale modelling to a typical radio-occultation profile exhibiting a night-time mixing layer[14,15]). The dust scenario used in the LMD-MMM simulations is derived from Thermal Emission Spectrometer observations for Martian Year 24 and interpolated using a kriging technique[49]. The static surface properties (topography, albedo, thermal inertia) in the mesoscale simulations are interpolated from high-resolution laser altimetry (MOLA) and thermal emission spectrometry (TES) on board Mars Global Surveyor available on the NASA Planetary Data System. The LMD-MMM simulations are carried out for four complete simulated Martian days, with the first two days serving as a spin-up for the mesoscale circulations and water cycle. The water-ice cloud spatial coverage and opacities reproduced by both the LMD-MGCM and the LMD-MMM in the simulations carried out in this paper are compliant with observations[17] and other MGCMs[12] (Supplementary Fig. 5). Mesoscale simulations are also capable of resolving the propagation of gravity waves and correctly replicating the mountain wave associated with Martian volcanoes in the Tharsis region[23,32].

Large-Eddy Simulations. To complement the above-mentioned regional-scale simulations, we use the LMD-MMM for turbulence-resolving simulations named Large-Eddy Simulations (LES)[50]. LES are employed, for example, to study convective motions in the PBL (ref. 19). In LES, the horizontal and vertical mesh spacing are refined towards 200 m to resolve the largest turbulent plumes, responsible for the majority of the transport of heat and momentum in convectively unstable conditions.

The spatial resolutions we adopt in the LMD-LES model are about a factor of 1,000 finer in the horizontal than in MGCMs, and a factor of 100 finer than in MMMs (in other words, a LMD-LES run could be regarded as a zoom within one grid point in a typical LMD-MMM run). Apart from the refined mesh spacing in the horizontal and in the vertical, LMD-LES runs differ from LMD-MMM runs by the use of periodical boundary conditions and uniform topography, albedo and thermal inertia. The initial conditions are generated by replicating on all grid points the same temperature profile extracted in a region, season and local time of interest from a MGCM simulation (Mars Climate Database (MCD) version 5.2). Consequently, the LES discussed in this work assume an almost uniform cloud cover over the LES domain—compliant with night-time observations of the cloud cover in the Ulysses Fossae plains enclosed by the Tharsis volcanoes and Olympus Mons[5,12] and LIDAR measurements on board Phoenix for the northern polar regions[36,37]. Addressing the impact of small-scale cloud inhomogeneities on the spatial structure of convective snowstorms is left as future work. Furthermore, our LES modelling does not account for the impact of a regional and/or global subsidence/upwelling on the local dynamics within the cloud (a question recently raised by observations by the Curiosity rover within Gale Crater[51]).

The physical packages used in the LMD-LES are exactly similar to the ones used in the LMD-MGCM and LMD-MMM as far as radiative transfer and cloud microphysics are concerned. The subgrid-scale parameterizations for turbulent mixing[29,30] employed in the LMD-MGCM and the LMD-MMM are not activated in LMD-LES integrations, where the largest turbulent eddies, responsible for mixing layers, are resolved (the sizes of the resolved convective plumes, much wider than the adopted horizontal resolution in our LES, act as an *a posteriori* justification for the choice of switching off parameterizations for turbulent mixing and using grid refinement towards what is typical of LES). Smaller-scale turbulent mixing, left unresolved even in LES, is handled with a Deardorff closure similarly to terrestrial LES performed with the WRF hydrodynamical solver[52].

We perform LMD-LES in a domain comprising $151 \times 151 \times 81$ grid points along the two horizontal and the vertical dimensions. The adopted grid spacing of 200 m entails a domain extent of 30 km in the horizontal and 15 km in the vertical. Refining the mesh spacing towards 100 m and 50 m only marginally changes the results obtained with the 200-m resolution runs (simulations with a spatial resolution of 1,000 m were also performed: the main characteristics of the convective plumes are analogous to those obtained with a 200-m LES run, although the convective structures are less finely resolved). The integration timestep is 3 s and the radiative and microphysical timesteps are both 60 s. The simulations do not benefit from a refinement of the microphysical timestep below 60 s, since our nucleation model[26] is formulated and designed to be used primarily in LMD-MMM and LMD-GCM with timesteps above 30 s.

Two types of LMD-LES experiments were carried out, both in northern summertime (heliocentric longitude $L_s = 120°–122°$). The first one corresponds to atmospheric conditions in the Ulysses Fossae high plateau (located in the Tharsis quadrangle of Mars: longitude $-120°$ E, latitude 8° N) where mixing layers were evidenced through radio-occultations[15]. The second one corresponds to atmospheric conditions in the landing site of the Mars Phoenix lander (located in Vasistas Borealis: longitude $-126°$ E, latitude 68° N) where fall streaks and virga were witnessed by the LIDAR on board Phoenix[36,37]. The LMD-LES computations are carried out from Martian dusk to dawn (local time 0800 PM to local time 0700 AM). In each type of LMD-LES experiments, the initial temperature profile at the relevant sites is extracted from the Mars Climate Database[53,54] (MCD) version 5.2, which compiles results obtained with the latest version of the LMD-MGCM[13,26]. The results obtained by LMD-LES at local times 0200–0500 AM differ only marginally from the reference case when an initial local time of 2200 PM or 0000 AM is used. A background wind profile of 15 m s^{-1} is set, to emulate a regional-scale wind in the LMD-LES model; not including such a background wind does not, however, change the intensity of the turbulent motions associated with the radiative destabilization in the water-ice cloud, and leave the morphologies of the simulated virga and fall streaks unaltered.

The initial tracer profiles for dust particles and water vapour in LMD-LES are also extracted from the MCD, with the initial water vapour mass mixing ratio and number density being obtained by adding the water vapour and water-ice cloud quantities. This allows for the cloud model[13,26] in the LMD-LES to predict the formation of water-ice clouds consistently with the profiles of temperature and dust particles computed at high vertical resolution in the LMD-LES, rather than relying on pre-existing clouds in the MCD profiles obtained from coarser-resolution GCM simulations. We checked that the cloud layers simulated in the LMD-LES runs (see left panels in Supplementary Figs 3 and 4) share the same properties as those

simulated by the LMD-MGCM and LMD-MMM. This can be also verified in the Ulysses Fossae experiment by comparing Fig. 2a,b.

We found it was difficult to form a water-ice cloud in the Phoenix LMD-LES experiment at the altitude of 4 km observed by the Phoenix LIDAR[36,37] at the heliocentric longitude $L_s = 122°$. The formation of this cloud is very sensitive to the local conditions of temperature and water vapour at the Phoenix landing site. Mesoscale modelling[48] showed that the transient dynamical activity is sustained in northern polar regions at $L_s = 120°$, which is consistent with the Phoenix LIDAR profiles not featuring a distinctive water-ice cloud in all the retrieved profiles[36,37] close to $L_s = 120°$. This regional dynamical activity is insufficiently resolved in the LMD-MGCM computations on which the MCD profiles are based; and LES modelling cannot account for the regional dynamics of a mesoscale model. To discuss the morphology and dynamics of the observed Phoenix cloud in our study, we ensured this cloud is formed in our LMD-LES model by decreasing the atmospheric temperature by 10 K in the initial profile extracted from the MCD, while leaving the water vapour profile unmodified. The volume mixing ratio for water vapour extracted from the MCD is similar to the value of 0.0014% inferred from the Phoenix observations[36,38].

Analysis of convective mixing resolved by LES. Convective mixing resolved by LES within and below water-ice clouds can be diagnosed with the approach adopted in LES studies of the PBL (ref. 19). Any physical quantity $\mathcal{Q}$ is split in its domain-averaged component $\langle\mathcal{Q}\rangle$ and fluctuating convective component $\mathcal{Q}' = \mathcal{Q} - \langle\mathcal{Q}\rangle$. The mixing layer resulting from resolved convective plumes by LES can be evidenced in the vertical profile of the domain-averaged potential temperature $\langle\theta\rangle$. The mechanism underlying convective mixing can be further assessed by computing the domain-averaged vertical profile of vertical eddy heat flux (or convective heat flux) $\langle w'\theta'\rangle$, where w is vertical velocity. Convection cools the atmosphere in layers within which $\langle w'\theta'\rangle$ increases with height, and warms the atmosphere in layers within which $\langle w'\theta'\rangle$ decreases with height. A positive value of $\langle w'\theta'\rangle$ denotes that the convective heat transfer is exerted mostly by warm updraughts ($w' > 0$ and $\theta' > 0$) and cold downdraughts ($w' < 0$ and $\theta' < 0$); a negative value of $\langle w'\theta'\rangle$ denotes that the convective heat transfer is dominated by warm downdraughts and cold updraughts. Just as convective heat transport is diagnosed by the vertical gradients of $\langle w'\theta'\rangle$, tracer transport in convective snowstorms can be diagnosed from our LES modelling by analysing vertical profiles of convective tracer transport $\langle w'q'\rangle$, where q is the volume mixing ratio of tracer (water vapour q_{vapour}, water ice q_{ice}, or total water $q_{tot} = q_{ice} + q_{vap}$). Convection acts to deplete the atmosphere of tracer q where $\langle w'q'\rangle$ increases with height, while a decrease of $\langle w'q'\rangle$ with height indicates a replenishment of tracer q by convective motions.

The domain-averaged vertical profiles of potential temperature $\langle\theta\rangle$, and convective transport of heat $\langle w'\theta'\rangle$ and tracers $\langle w'q'\rangle$, are shown in Supplementary Fig. 3 (Ulysses Fossae conditions, see Fig. 2b) and Supplementary Fig. 4 (Phoenix lander's Vasitas Borealis conditions, see Fig. 3b). The vertical profiles of $\langle q_{ice}\rangle$ and $\langle q_{vapour}\rangle$ indicate the water-ice cloud layer and the hygropause. As is evidenced in the vertical profile of potential temperature $\langle\theta\rangle$, a nearly neutral deep layer is produced within and below the water-ice cloud in both LES case studies. The mixing layer reproduced in the Ulysses Fossae LES shares the same characteristics (a 8-km vertical extent within and below a 3-km-deep water-ice cloud occurring 10 km above the surface) as the mixing layer evidenced by radio-occultations[15] (Fig. 1b) and reproduced in the mesoscale simulations using parameterized mixing (Fig. 1c and Fig. 2b). The Vasitas Borealis LES case, run to compare to Phoenix LIDAR observations, exhibits a shallower 2.5-km-deep mixing layer than the Ulysses Fossae case.

The profiles of convective transport of heat, water vapour and water ice in the mixing layer is similar in the two LES cases. The domain-averaged vertical profile of $\langle w'\theta'\rangle$ demonstrates that the mixing layer results from cold downdraughts and warm updraughts, which warm the atmosphere in the upper half of the mixing layer (where the strongest radiative cooling is exerted by the water-ice particles, see Supplementary Fig. 1) and cool it in the lower half of the mixing layer. This mixing layer is overlain by an entrainment layer cooled by overshooting updraughts and underlain by an entrainment layer warmed by overshooting downdraughts (this bottom entrainment layer is more prominent in the Ulysses Fossae case than in the Phoenix case). The top entrainment layer is also found in terrestrial and Martian PBL daytime convection[19]; the bottom entrainment layer has no counterpart in terrestrial and Martian PBL. Interestingly, this three-layer structure associated with cloud-induced convective motions on Mars is analogous to the one obtained recently by LES modelling of Venus' convective cloud layer (compare Supplementary Fig. 3 to Fig. 6 in ref. 55). This provides further grounds for the analogy, mentioned in the main text, between convective motions in Venusian and Martian clouds.

The vertical profile of $\langle w'q'_{ice}\rangle$ supports that convective motions within and below the water-ice clouds cause a depletion of water ice within the cloud in favour of the region below the cloud, that is, a downward convective transport of water ice. The negative sign of $\langle w'q'_{ice}\rangle$ indicates that this convective transport results from ice-rich downdraughts coming from the cloud (what we name ice microbursts) and ice-poor updraughts coming from below the cloud. Conversely, the vertical profile of $\langle w'q'_{vapour}\rangle$ indicates that the action of vapour-rich updraughts and vapour-poor downdraughts cause a depletion of water vapour below the hygropause in favour of a replenishment of water vapour within the cloud, above the hygropause. The vertical profiles of the convective transport of total water $\langle w'q'_{tot}\rangle$ indicate a depletion of water by convective motions in the whole cloud-induced mixing layer. Our LES modelling thereby suggests that the net effect of night-time convective snowstorms on Mars is to transport water outside of the mixing layer. Our simulations do not allow us to determine whether this transport is occurring downwards or upwards (that is, in favour of an underlying or overlying layer with $\langle w'q'_{tot}\rangle$ increasing with height). Net downward convective transport of water is found in the Ulysses Fossae LES case (Supplementary Fig. 3), suggesting confinement of water in the near-surface atmosphere; conversely, net upward transport is found in the Phoenix LES case (Supplementary Fig. 4), suggesting transport towards the higher troposphere. A broader diversity of convective snowstorms shall be explored to determine the net convective transport of total water by Martian convective snowstorms on the regional to global scales.

References

43. Forget, F. et al. Improved general circulation models of the Martian atmosphere from the surface to above 80 km. J. Geophys. Res. **104,** 24155–24176 (1999).
44. Hourdin, F. A new representation of the CO₂ 15 μm band for a Martian general circulation model. J. Geophys. Res. **97,** 18319–18335 (1992).
45. Madeleine, J.-B., Forget, F., Millour, E., Montabone, L. & Wolff, M. J. Revisiting the radiative impact of dust on Mars using the LMD Global Climate Model. J. Geophys. Res. **116,** E11010 (2011).
46. Määttänen, A. et al. Nucleation studies in the Martian atmosphere. J. Geophys. Res. **110,** E02002 (2005).
47. Colaïtis, A. et al. A thermal plume model for the Martian convective boundary layer. J. Geophys. Res. **118,** 1468–1487 (2013).
48. Tyler, D. & Barnes, J. R. Atmospheric mesoscale modeling of water and clouds during northern summer on Mars. Icarus **237,** 388–414 (2014).
49. Montabone, L. et al. Eight-year climatology of dust optical depth on Mars. Icarus **251,** 65–95 (2015).
50. Lilly, D. K. On the numerical simulation of buoyant convection. Tellus **14,** 148–172 (1962).
51. Tyler, D. & Barnes, J. R. Mesoscale modeling of the circulation in the Gale Crater region: an investigation into the complex forcing of convective boundary layer depths. Mars **8,** 58–77 (2013).
52. Moeng, C. H., Dudhia, J., Klemp, J. & Sullivan, P. Examining two-way grid nesting for Large Eddy Simulation of the PBL using the WRF model. Mon. Weather Rev. **135,** 2295–2311 (2007).
53. Lewis, S. R. et al. A climate database for Mars. J. Geophys. Res. **104,** 24177–24194 (1999).
54. Millour, E. et al. & MCD/GCM Development Team The Mars Climate Database (MCD Version 5.2) (European Planetary Science Congress, EPSC2015-438, 2015).
55. Lefèvre, M., Spiga, A. & Lebonnois, S. Three-dimensional turbulence-resolving modeling of the venusian cloud layer and induced gravity waves. J. Geophys. Res. **122,** 134–149 (2017).